

How electron two-stream instability drives cyclic Langmuir collapse and continuous coherent emission

Haihong Che^{a,b,1}, Melvyn L. Goldstein^b, Patrick H. Diamond^c, and Roald Z. Sagdeev^d

^aDepartment of Astronomy, University of Maryland, College Park, MD 20742; ^bHeliospheric Physics Laboratory, NASA Goddard Space Flight Center, Greenbelt, MD 20771; ^cDepartment of Physics, University of California, San Diego, La Jolla, CA 92093; and ^dDepartment of Physics, University of Maryland, College Park, MD 20742

Edited by Neta A. Bahcall, Princeton University, Princeton, NJ, and approved December 27, 2016 (received for review August 23, 2016)

Continuous plasma coherent emission is maintained by repetitive Langmuir collapse driven by the nonlinear evolution of a strong electron two-stream instability. The Langmuir waves are modulated by solitary waves in the linear stage and electrostatic whistler waves in the nonlinear stage. Modulational instability leads to Langmuir collapse and electron heating that fills in cavitons. The high pressure is released via excitation of a short-wavelength ion acoustic mode that is damped by electrons and reexcites small-scale Langmuir waves; this process closes a feedback loop that maintains the continuous coherent emission.

electron beams | nonlinear wave interaction | Langmuir collapse | coherent emission | plasma turbulence

Electron beams accelerated by solar flares and nanoflares are believed to be responsible for several types of solar radio bursts observed in the corona and interplanetary medium, including flare-associated coronal type U and J and interplanetary type III radio bursts, and nanoflare-associated weak coronal type III bursts (1–4). In 1958, Ginzburg and Zhelezniakov first proposed a basic framework for such bursts, which was subsequently refined by others (refs. 5 and 6 and references therein). In essence, the scenario is one in which the electron two-stream instability (ETSI), driven by electron beams, generates Langmuir waves that are converted into plasma coherent emission via nonlinear three-wave coupling [e.g., two Langmuir waves and one ion acoustic wave (IAW)]. However, the mechanism whereby the nonlinear ETSI produces coherent emission with a duration of several orders of magnitude longer than the linear saturation time is not well understood (6–9). Nonlinear evolution of ETSI is a fundamental problem in nonlinear wave theory in which disparate three-wave couplings dominate the energy transport and dissipation (10). It has broad applications in plasma physics, planetary physics, and astrophysics, such as terahertz emission in laser beam experiments, radio bursts from Jupiter, pulsars, and the formation of exotic astrophysical objects.

In the classical Kolmogorov turbulence scenario, the balance between energy input and its final absorption is controlled by a nonlinear cascade from large spatial scales (the region of external forcing) to viscosity-dominated short wavelengths. In plasmas, the source of instability is often beams of charged particles that generate Langmuir waves. At shorter wavelengths, the natural candidate to provide the sink of wave energy is Landau damping. However, nonlinear disparate wave interactions, it follows from direct calculation of basic three-wave coupling, can only lead to inverse cascades (to longer wavelengths) through modulational instability (11), and away from the Landau damping region of the spectrum. The eventual nonlinear process capable of overriding this inverse cascade was suggested by Zakharov, namely Langmuir collapse (LC), which is analogous to a self-focusing of the Langmuir waves packets, or cavitons (12, 13). LC has been discovered in both experiments and space observations (14–16); in particular, LC has been observed in association with solar radio bursts (15–17).

There are several problems with the current models of type III radio bursts. The most important physics missed is the feedback of LC that, we will show, plays a critical role in maintaining continuous coherent emission. Second, the existing models (ref. 6 and references therein) use a common assumption that we call “weak turbulence condition,” specifically, the growth rate of Landau fluctuation driven by an electron beam is much smaller than that of the ETSI, or $v_{te,c} < v_b < (n_c/n_b)^{2/3} v_{te,b}$, where v_b is the electron beam drift, $v_{te,c}$ and $v_{te,b}$ are the thermal velocity of core background electrons and beams, respectively, and n_c/n_b is the core-beam density ratio. However, recent observations suggest that the electron beam density near coronal source regions is comparable to the background density (18). Thus, the weak turbulence condition can be significantly violated. Third, the models assume that the emission is produced by coupling between Langmuir waves and IAWs, but IAWs are expected to be heavily damped in the nearly isothermal plasma of the corona.

We here present a mechanism based on a model of cyclic LC and Langmuir wave regeneration. The results of massive particle-in-cell (PIC) simulations of the ETSI show how the nonlinear ETSI produces coherent emission that lasts five orders of magnitude longer than the linear saturation time. As shown in Fig. 1, the extended emission time is a consequence of repeated LC, which regenerates Langmuir waves through resonance with intermediary short-wavelength IAWs. The short-wavelength IAW is produced due to the release of the ions inside the caviton caused by LC. Near the linear saturation of the ETSI, LC is initiated by the interactions between the high-frequency Langmuir waves produced in the background and the low-frequency Langmuir waves in the solitary wave-trapped electrons. As the ETSI enters the nonlinear decay, LC regenerates Langmuir waves, interacts with electrostatic (ES) whistler waves, and reinitiates LC, thus forming a feedback loop. ES whistler waves are sustained by electromagnetic (EM) kinetic Alfvén waves (KAWs)

Significance

Electron two-stream instability (ETSI) is believed to be responsible for the radio bursts observed in both the solar corona and interplanetary medium. What nonlinear kinetic processes self-consistently reconcile the several orders of magnitude difference between the short linear saturation time scale of ETSI and the long duration of bursts is fundamental in plasma turbulence and has remained unsolved for nearly 50 y. Using massive particle-in-cell simulations, we find a self-consistent and complete nonlinear solution to this problem.

Author contributions: H.C. and M.L.G. designed research; H.C. performed research; H.C., M.L.G., P.H.D., and R.Z.S. analyzed data; and H.C., M.L.G., P.H.D., and R.Z.S. wrote the paper.

The authors declare no conflict of interest.

This article is a PNAS Direct Submission.

¹To whom correspondence should be addressed. Email: chehh06@gmail.com.

This article contains supporting information online at www.pnas.org/lookup/suppl/doi:10.1073/pnas.1614055114/-DCSupplemental.

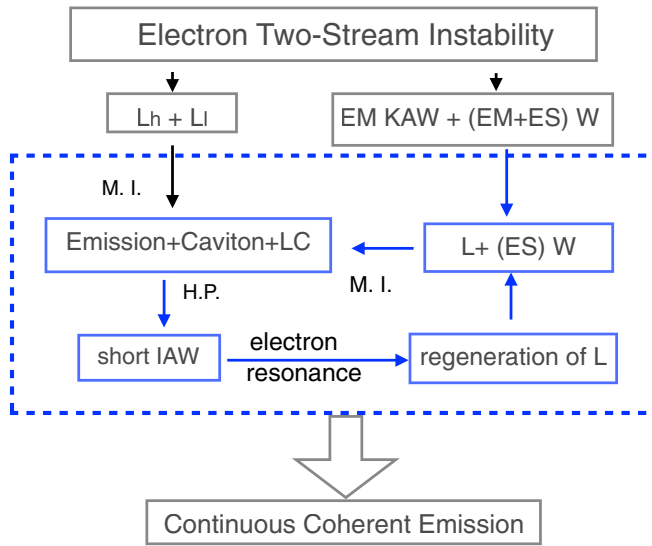


Fig. 1. Schematic diagram showing how LC, occurring during the nonlinear stage of the ETSI, forms a feedback loop (within the blue-dashed line box) that produces coherent emission continuously. H.P., high pressure; L, Langmuir wave; L_h , Langmuir wave with higher frequency produced by the background electrons; L_l , Langmuir wave with lower frequency produced by the trapped electrons in solitary waves; M.I., modulational instability; W, Whistler wave.

and whistler waves that are produced simultaneously with the Langmuir waves. The structure of this paper is as follows: we first present the simulation results on the generation and regeneration of LC and emission during the nonlinear stage of ETSI. We then give the governing equations and condition for LC. Finally, we show how LC regenerates Langmuir waves.

Simulation Results of Cyclic Emission

The initialization of 2.5D PIC simulation is described in the caption of Fig. 2. The ratio between the initial beam velocity and the thermal velocity $v_{bd,0}/v_{te,0} \approx 12 > (n_c/n_b)^{2/3} \approx 5$, where $v_{te,0}$ is the initial thermal velocity of both core and beam electrons, guarantees a strong ETSI. The total simulation time is $\omega_{pe,0}t = 14,400$, during which ETSI experiences a linear and nonlinear stage, saturation, and nonlinear decay, and eventually reaches turbulent equilibrium, where the energy exchange between particles and waves reaches balance (19).

The growth stage of ETSI includes the linear and nonlinear stage ($\omega_{pe,0}t = 0$ to 200). The saturation stage is from $\omega_{pe,0}t \approx 200$ to 1,000. The linear stage only lasts for $\omega_{pe,0}t = 2$ as defined by the growth rate of the ETSI from quasi-linear theory [i.e., $\gamma = \sqrt{3}/2(n_{b0}/n_{c0})^{1/3}\omega_{pe,0} \approx 2\omega_{pe,0}$]. During the growth stage, the large beam drift suppresses the generation of Langmuir waves (20). The fastest-growing mode of the solitary wave has $k_x\lambda_{De,0} \approx v_{te,0}/v_{bd,0} \approx 0.1$ and $\omega/\omega_{pe,0} \approx (n_{b0}/n_{c0})^{1/3}\omega_{pe,0} \approx 0.5\omega_{pe,0}$ as shown in Figs. 2A and 3A. Quickly, the ETSI loses $\sim 85\%$ of the kinetic energy of the beams and reaches saturation with the beam drift v_{db} being about 2 times the core thermal velocity $\sim 2v_{te,c}$ to $\sim 30v_{A,0}$. The thermal velocity of the electron beams $v_{te,b}$ increases to $40v_A$ and a bump forms at the tail of the core electron velocity distribution function (21). The core-beam density ratio changes to $n_b/n_c \approx 0.05$. The ratio $v_{bd,0}/v_{te,b} \approx 0.7 < (n_c/n_b)^{2/3} \approx 3$ indicates that the ETSI becomes weak turbulence. The bump starts to excite Langmuir waves as well as coherent emission (Figs. 2B and 3B). The backward propagating Langmuir waves with frequency near $\omega_{pe,0}$ are excited in the background plasma while the propagating forward Langmuir waves with frequency near $0.6\omega_{pe,0}$ are excited by the

trapped electrons due to the low density and high temperature in the electron potential well (22). These two Langmuir waves satisfy the following dispersion relation (normalized by the initial $\omega_{pe,0}$ and $\lambda_{De,0}$):

$$\frac{\omega}{\omega_{pe,0}} = \left(\frac{n_c^2}{n_0^2} + \frac{T_{ce}n_e}{T_{ce,0}n_0} \gamma k_x^2 \lambda_{De,0}^2 \right)^{1/2}, \quad [1]$$

where $\gamma = 3$, as the electron heating caused by the solitary wave, is nearly adiabatic (23).

The coalescence of the two antiparallel Langmuir waves drives modulational instability and leads to LC (11, 12), accompanied by a harmonic emission with $\approx 1.6\omega_{pe,0}$ (Supporting Information). The emission is shown in Fig. 3B, propagating much more strongly forward than backward and satisfying the dispersion relation

$$\frac{\omega}{\omega_{pe,0}} = \left(\frac{n_c^2}{n_0^2} + \frac{c^2}{v_{te}^2} k_x^2 \lambda_{De,0}^2 \right)^{1/2}. \quad [2]$$

The LC leads to the contraction of the modulated Langmuir envelope and the formation of ion density cavitons (see Movie S1). We plot a sample of parallel electric field E_x in Fig. 4A–C at three moments: $\omega_{pe,0}t = 72, 320$, and 680. At $\omega_{pe,0}t = 72$, the solitary waves with wavelength near the fastest-growing mode reach the peak. The critical condition for LC $E^2/8\pi n_0 T_e > \frac{1}{4}k_x^2 \lambda_{De}^2$ is satisfied because $(E^2/8\pi n_0 T_e)^{1/2} \approx 0.4$ with $E/E_0 \approx 50$ is larger than the fastest-growing mode of the ETSI $k\lambda_{De}/2 \approx v_{te,0}/2v_{db,0} \approx 0.05$. At $\omega_{pe,0}t = 320$, the modulated wave envelopes decrease from 50 to 30 $\lambda_{De,0}$, and ion density cavitons form. In Fig. 4D, we show an example of caviton in the xy plane for the Langmuir envelope plotted in red in Fig. 4B (see Movie S1). Contraction of the

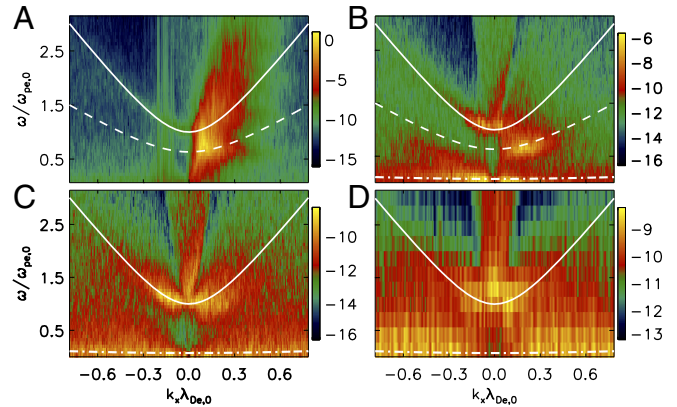


Fig. 2. The $\omega/\omega_{pe,0}-k_x\lambda_{De,0}$ diagrams of the parallel propagating high-frequency electric field component E_x at four time intervals: (A) $\omega_{pe,0}t = 0-100$, (B) $\omega_{pe,0}t = 320-420$, (C) $\omega_{pe,0}t = 2,880-2,980$, and (D) $\omega_{pe,0}t = 10,560-10,580$. Also shown are the dispersion relations (Eq. 1) of the background electrons (solid lines), trapped electrons (dashed lines), and the short-wavelength IAW (dash-dotted lines). For the waves in space, see Figs. S1–S3. The 2.5D PIC simulation is initialized with a homogeneous plasma and uniform magnetic field $\mathbf{B} = B_0\hat{x}$. The initial ion velocity distribution function is a single Maxwellian and the electron velocity distribution function is core-beam bi-Maxwellian (19). The initial density ratio of the beam and core is $n_{b0}/n_{c0} = 0.1$, and the core and beam temperatures $T_{b,0} = T_{c,0}$. The initial drifts of the core $v_{cd,0}$ and the beam $v_{bd,0}$ satisfy $(1 - \delta)v_{cd,0} = -\delta v_{bd,0}$ to maintain null current; $v_{bd,0} = 12v_{te,0} = 60v_{A,0}$, where $v_{A,0}$ is the initial Alfvén speed and $v_{te,0} = (kT_{c,0}/m_e)^{1/2}$. The speed of light $c = 100v_{A,0}$ and $m_i/m_e = 100$. The ion temperature $T_{i,0} = T_{c,0}$. The boundaries are periodic, and the box size $L_x = L_y = 3,200\lambda_{De,0}$ ($\lambda_{De,0} \equiv v_{te,0}/\omega_{pe,0}$), where $\omega_{pe,0}$ is the initial electron plasma frequency. The electric field is normalized by $E_0 = v_{A,0}B_0/c$; $\beta = 16\pi kT_{c,0}/B_0^2 = 0.25$.

Langmuir wave envelopes efficiently dissipates the Langmuir wave energy into electron thermal energy because the rate of Landau damping is proportional to $n_b \omega_{pe}^3 / n_0 v_{te,b}^2 k^2$ (20). The electron temperature along the magnetic field T_{ex} inside the caviton is shown in Fig. 4E. The increased pressure inside the caviton releases the excess density and produces an intermediary short IAW with frequency ω_{pi} (dash-dotted line in Fig. 2B). The time scale for the growth of caviton is consistent with the modulation instability growth rate $\omega_{pi} (\langle E^2 \rangle / 8\pi n_0 T_e)^{1/2} \approx 0.01 \omega_{pe}$. At $\omega_{pe,0} t = 680$, some wave envelopes continue to contract to wavelengths about $10 \lambda_{De,0}$, whereas some collapses lead to the vanishing of cavitons.

With the onset of LC, ETSI enters the nonlinear decay stage at $\omega_{pe,0} t \approx 1,000$. The LC in saturation stage causes the two antipropagating Langmuir waves to merge into a single Langmuir wave with frequency $\approx \omega_{pe,0}$ (Fig. 2C). Simultaneously, both whistler and kinetic KAW are generated, which were investigated in a previous study (19). The whistler wave dispersion relation $\omega = v_A^2 k k_{\parallel} / \Omega_{ci} + \Omega_{ci}$ (24) indicates that the whistler wave has ES component with a frequency of $\sim 0.001 \omega_{pe,0}$ and is strongly affected by density (Fig. 5A and B). In Fig. 5C and D, we show both the electron and ion density fluctuations in (ω, k) phase space and find that both agree with the dispersion relation of ES whistler waves (W_s). Plasma fundamental emission (Fig. 3C) is produced through both coalescence $L + W_s \rightarrow T$ and decay $L \rightarrow T + W_s$, where T is the transverse emission. A new Langmuir wave L' is produced through $L + W_s \Rightarrow L'$. The coalescence $L + L' \Rightarrow T$ is much weaker because it is a second-order process. As a result, harmonic emission in this stage is not identifiable.

The ETSI reaches nonlinear saturation around $\omega_{pe,0} t \approx 10,000$. The wavelength of Langmuir wave and ion caviton becomes longer and EM emission is produced in a broad range of frequencies and wavenumbers (Figs. 2D and 3D), which is a consequence of repeating LC maintained by the feedback loop shown in Fig. 1 (see Movie S2). The turbulent fluctuations of density and electric field in phase space increase to levels comparable to that of the Langmuir waves and emissions. The emission reaches its balance between the plasmons of Langmuir waves and whistler waves—the Manley–Rowe relation—and the coupling becomes $L + W_s \Rightarrow T$ (25, 26). During this stage, electrons are strongly heated and scattered, and the initial anisotropic electron beams become an isotropic halo population superposed over the core electron distribution function (21).

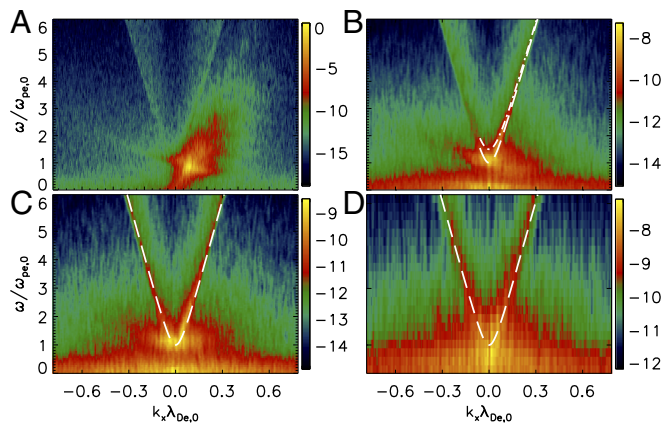


Fig. 3. The $\omega/\omega_{pe,0}-k_x \lambda_{De,0}$ diagrams of parallel propagating high-frequency E_y are shown for the same four time intervals as for Fig. 2. (A) $\omega_{pe,0} t = 0-100$, (B) $\omega_{pe,0} t = 320-420$, (C) $\omega_{pe,0} t = 2,880-2,980$, and (D) $\omega_{pe,0} t = 10,560-10,580$. Dashed lines denote dispersion relation of plasma emission with frequency $\approx \omega_{pe,0}$. Dash-dotted line in B is dispersion relation of plasma emission with frequency $\omega/\omega_{pe,0} = 1.6$.

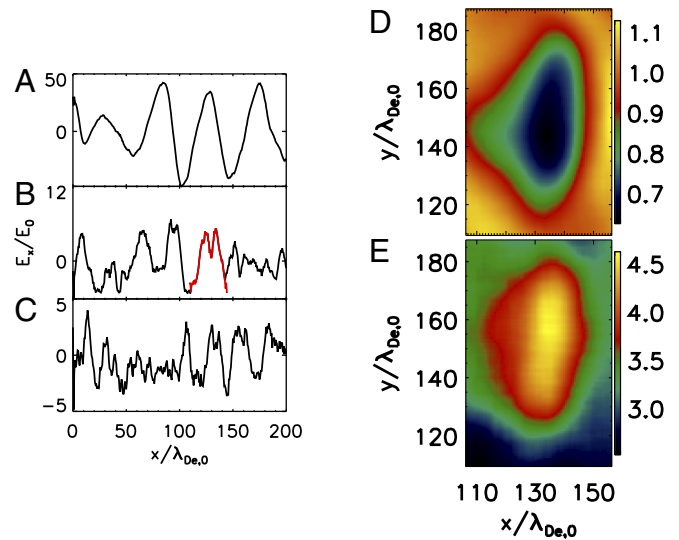


Fig. 4. (A–C) The parallel electric field E_x cuts for $x \in [0, 200] \lambda_{De,0}$ and $y = 100 \lambda_{De,0}$ at (A) $\omega_{pe,0} t = 72$ when the ETSI nearly saturates and hot electrons excites Langmuir waves; (B) $\omega_{pe,0} t = 320$ when the modulational instability grows, LCs start, and cavitons form; and (C) $\omega_{pe,0} t = 648$ when LCs continue. (D) The ion density in xy plane, i.e., the caviton, and (E) the electron temperature in x direction T_{ex} inside the caviton corresponding to the Langmuir envelope in red in B (see Movie S1).

L– W_s Coupling and LC

The ES component of whistler wave, that is, the ES whistler wave with frequency of several Ω_{ci} and wavelength $k \lambda_{De} \ll 1$, defines a slow time scale and a large spatial scale, whereas the Langmuir wave defines a fast time scale and small spatial scale $k \lambda_{De} \approx 1$. The coupling between ES whistler waves and Langmuir waves drives modulational instability that leads to the formation of long-wavelength Langmuir envelopes $\mathbf{E}_L(\mathbf{x}, t)$ and cavitons. Langmuir waves exert a low-frequency ponderomotive force on the motion of electrons and ions and mediate their interaction with whistler waves in a manner similar to L–IAW coupling (11, 12). The difference here is that whistler waves are produced in magnetized plasmas whereas IAWs are less sensitive to magnetic fields. The ES whistler wave is associated with EM whistler wave and cannot independently exist. In the following, we show this difference and why it does not significantly affect the critical condition for LC. Assuming perturbations $\mathbf{E} = \mathbf{E}_s + \mathbf{E}_L$, $\mathbf{v} = \mathbf{v}_s + \mathbf{v}_L$, $n_e = n_0 + \delta n_L + \delta n_s$ and $\delta n_i \approx \delta n_s$, where the subscripts L and s represent fast and slow time scales, respectively. Neglecting the high-frequency interactions, we have the same driven equation as for the L–IAW coupling (12),

$$\frac{i}{\omega_{pe,0}} \frac{\partial \mathbf{E}_L}{\partial t} + \frac{\gamma v_{te}^2}{4\omega_{pe,0}^2} \nabla^2 \mathbf{E}_L - \frac{\delta n_s}{2n_0} \mathbf{E}_L = 0. \quad [3]$$

On the slow time scale, ions play the same role as electrons in maintaining the cavitons. In Fig. 5, both the ion and electron density fluctuations propagate at the phase speed of whistler waves $\sim 3v_A$, $\sim 6v_{ti}$, and $\sim 0.2v_{te}$. The slow component of electron and ion motions in a magnetized plasma can be described by the following equations:

$$\frac{\partial \mathbf{v}_s}{\partial t} + (\mathbf{v}_s \cdot \nabla) \mathbf{v}_s + \frac{e}{m_e} \mathbf{E}_s + \frac{e}{m_e c} \mathbf{v}_s \times \mathbf{B}_0 + \frac{\gamma_e T_e}{n_0 m_e} \nabla \delta n_s + \frac{1}{m_e n_0} \nabla \phi_{pm} = 0, \quad [4]$$

$$\frac{\partial \mathbf{v}_i}{\partial t} + (\mathbf{v}_i \cdot \nabla) \mathbf{v}_i - \frac{e}{m_i} \mathbf{E}_s - \frac{e}{m_i c} \mathbf{v}_i \times \mathbf{B}_0 + \frac{\gamma_e T_i}{n_0 m_i} \nabla \delta n_s + \frac{m_e}{m_i^2 n_0} \nabla \phi_{pm} = 0, \quad [5]$$

where $\phi_{pm} \equiv |E_L|^2/16\pi$, and $\nabla \phi_{pm}$ is the ponderomotive force. Eliminating \mathbf{E}_s and using the approximation $m_e \mathbf{v}_s/m_i + \mathbf{v}_i \approx \mathbf{v}$, together with the ion continuity equation, $\partial(m_e + m_i)\delta n_s/\partial t + n_0(m_e + m_i)\nabla \cdot \mathbf{v} = 0$, we obtain

$$\frac{\partial^2 \delta n_s}{\partial t^2} \frac{1}{n_0} - c_s^2 \nabla^2 \frac{\delta n_s}{n_0} - M = \nabla^2 \frac{\phi_{pm}}{n_0 m_i}, \quad [6]$$

where $M = \mathbf{B}_0 \cdot \nabla \times \mathbf{j}/(m_i n_0 c)$ is the modulation of the magnetic field that excites the whistler wave, $\mathbf{j} = en_0(v_i - v_s)$ is the current density, and $c_s^2 \approx (\gamma_e T_e + \gamma_i T_i)/m_i$ is the phase speed of the IAW. In a homogeneous plasma, to first order, the current density is caused by the polarization drift, i.e., $\mathbf{j} \approx [(m_e + m_i)n_0/B_0^2] \partial \mathbf{E}_s / \partial t$. The curl in M implies that ES whistler waves originate from the perpendicular EM components of whistler waves and KAWs (22). In other words, the density fluctuations on the slow time scale are mediated predominantly by the EM whistler and KAW waves, and the influence of M is small. We will neglect M when discussing the modulational instability and the critical condition of LC.

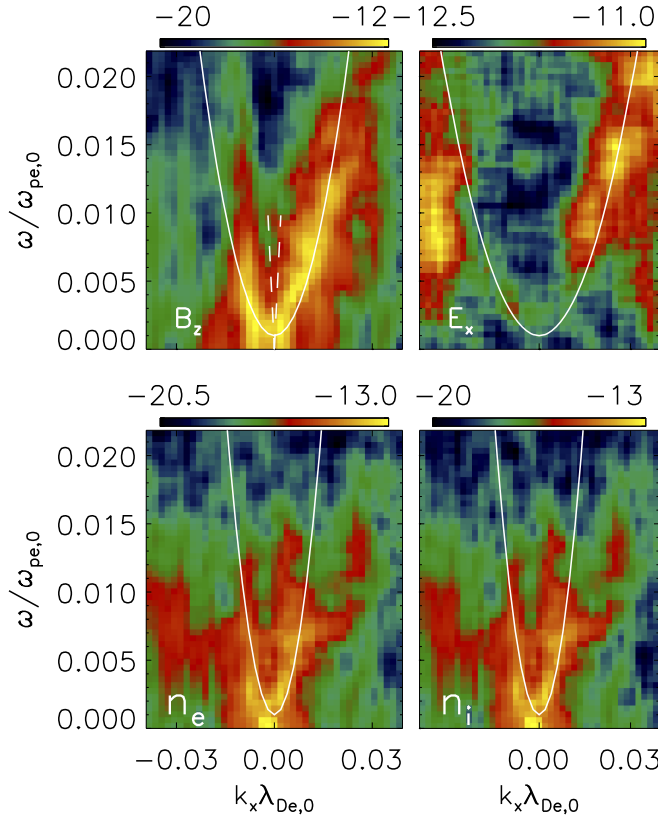


Fig. 5. The $\omega/\omega_{pe,0}-k_x\lambda_{De,0}$ diagram of parallel propagating low-frequency fluctuations of B_z , E_x , density n_e , and density n_i . The data are from $\omega_{pe,0}t = 720$ to $14,400$. Solid line denotes the dispersion relation of whistler wave; Dashed line denotes the dispersion relation of parallel propagating KAW. The details on the generation of KAWs and whistler waves by the nonlinear ETSI can be found in ref. 19.

From Eqs. 3 and 6, the maximum growth rate for modulational instability is $\gamma_m = \omega_{pi}(\langle E_L^2 \rangle / 8\pi n_0 T_e)^{1/2}$, and the critical condition for LC is (12)

$$\frac{E_L^2}{8\pi n_e T_e} > \frac{1}{4} k_x^2 \lambda_{De}^2. \quad [7]$$

In the nonlinear stage, the time scale of the modulational instability becomes longer than it is in linear saturation, due to the decrease of the electric field, but $(E^2/8\pi n_e T_e)^{1/2} \approx 0.2$ is still larger than the typical Langmuir wavenumber $k\lambda_{De}/2 \approx 0.05$ for the ES whistler waves, indicating LC can repeatedly occur.

Regeneration of Langmuir Waves

LC transfers energy from large to small scales, inverse to the modulational instability. Repeating LC requires regeneration of Langmuir waves so that $L-W_s$ coupling can continue to produce emission (Fig. 1).

In Eq. 6, ions fill the cavitons and excite short-wavelength IAWs (27) when the balance between the thermal pressure and radiation pressure is lost and Langmuir envelopes collapse. The dispersion relation of IAWs with thermal correction under the condition $v_{ti} < w/k < v_{te}$ is

$$1 + \frac{1}{k^2 \lambda_{De}^2} - \frac{\omega_{pi}^2}{\omega^2} \left(1 + \frac{3k^2 v_{ti}^2}{\omega^2} \right) = 0, \quad [8]$$

where the term $3k^2 v_{ti}^2/\omega^2$ in the bracket comes from the first-order expansion of the ion zeta function $Z(w/k/v_{ti})$, a higher order correction for the case $w/k/v_{ti} > 1$, but not $\gg 1$.

For short-wavelength IAWs with $k\lambda_{De} \approx 1$ in a plasma with $T_i \approx T_e$, the dispersion relation becomes

$$\omega^2 \approx \omega_{pi}^2 \frac{1 + \sqrt{3T_i/T_e}}{4} + \sqrt{\frac{3T_e}{T_i}} k^2 v_{ti}^2, \quad [9]$$

and, for long-wavelength $k\lambda_{De} \ll 1$,

$$\omega = \pm \sqrt{\frac{T_e}{m_i}} k. \quad [10]$$

Eq. 9 shows that the phase speed of short-wavelength IAWs satisfies $\omega^2/k^2/v_{ti}^2 \approx 1/k^2 \lambda_{De}^2$, and thus, for the short-wavelength IAW with a few tenths $k\lambda_{De}$, the exponential ion damping rate is comparable to electrons, and the rate is $\gamma_{ia} \approx (m_e/m_i)^{1/2} \omega_{pi}/k^3 \lambda_{De}^3$. The dissipation of the short-wavelength IAW is slower by a factor of $\gamma_{ia}/\gamma_m \approx (m_e/m_i)^{1/2}$ than the modulational instability, and thus this wave can be observed (Fig. 2 B–D). On the other hand, the damping rate of long-wavelength IAW is too strong to maintain L -IAW coupling and is suppressed by L - W_s coupling.

During LC, the wave energy is transferred from long-wavelength Langmuir waves to short-wavelength IAWs and then is returned to the newly generated short-wavelength Langmuir waves. Such energy transfer can be shown in the phase space (ω, k) using quasi-particle (plasmon) description. The plasmon number is defined as $N = E_k/\omega_k$, where E_k is the energy density of Langmuir envelope and $N(k, x, t)$ is the number of plasmons (26). The evolution of the mean plasmon number $\langle N(k, x, t) \rangle$ in phase space during wave interactions is determined by the wave self-interactions and wave-wave interactions,

$$\frac{d\langle E_k \rangle}{dt} = -\mathbf{v}_g \cdot \mathbf{D} \cdot \frac{\partial \langle N \rangle}{\partial \mathbf{k}}, \quad [11]$$

where the group velocity $\mathbf{v}_g = \partial\omega/\partial\mathbf{k}$, phase space diffusion coefficient $\mathbf{D} = \mathbf{q}\mathbf{q} \int \int_{\mathbf{q}, \Omega} i\omega_{pe,0}^2 \delta n_s^2 / (\Omega - \mathbf{q} \cdot \mathbf{v}_g + i\hat{\Gamma}) d\mathbf{q} d\Omega$, Γ is the self-interaction of Langmuir wave, the primary part $\langle \Gamma \rangle$ is associated with the mean plasmon number $\langle N \rangle$, and $\hat{\Gamma}$ is the first-order self-nonlinearity of Langmuir wave, such as linear growth

Table 1. Model predictions and observational evidence

Model predictions	Observations	Refs.
In the solar corona, emission duration $\approx 10^5 \omega_{pe}^{-1} \approx 1 - 10$ ms	Coronal type J and U radio bursts	(3, 4, 31)
Langmuir waves and whistler waves	Weak coronal type III radio bursts	(16, 32, 33)
Langmuire collapse and short wavelength IAW	Interplanetary type III radio bursts	(15, 34, 35)

or damping, where \mathbf{q} and Ω are the wave vector and frequency of IAWs, respectively.

In the case of linear growth $\hat{\Gamma} \approx 0$, a second instability can occur at $\Omega \simeq \mathbf{q} \cdot \mathbf{v}_g$. If $\mathbf{q} \cdot \partial \langle N \rangle / \partial \mathbf{k} |_{\Omega} > 0$, we have $dE_k/dt < 0$, indicating the energy transfers from the Langmuir wave to IAWs. The Langmuir wave is depleted by the Landau damping of caviton trapped wave-scattering, and the short-wavelength IAWs repopulate the energy of the short-wavelength part of the energy distribution. If $\mathbf{q} \cdot \partial \langle N \rangle / \partial \mathbf{k} |_{\Omega} < 0$, we have $dE_k/dt > 0$, indicating the regeneration of Langmuir waves. The short-wavelength IAW is damped by electrons, and the hot electrons reproduce the short-wavelength Langmuir waves.

The short-wavelength IAW acts as an intermediary wave in the regeneration of Langmuir waves. The Langmuir wave energy gain by modulational instability and loss by LC can reach a balance, i.e., $\gamma_{ia} W_{ia} = \gamma_m W_L$, where the short-wavelength IAW wave energy density $W_{ia} = n_0 T_e \sum_k \delta n_{s,k}^2 / n_0$, the short-wavelength Langmuir wave energy density $W_L = \langle E_L^2 \rangle (k_0/k)^{3/2} / 8\pi$, and $k_0 = 1/\lambda_{De} (\langle E_L^2 \rangle / 8\pi T_e)^{1/2}$ —the critical Langmuir wavenumber corresponding to LC at which the short-wavelength IAW energy is transferred into short-wavelength Langmuir waves (27).

The electron resonance with the short-wavelength IAWs reexcites Langmuir waves with a frequency shift, and Eq. 3, when modified to include the short-wavelength IAW excitation (27), becomes

$$\begin{aligned} \frac{i}{\omega_{pe,0}} \frac{\partial \mathbf{E}_L}{\partial t} + \frac{\gamma v_{te}^2}{4\omega_{pe,0}^2} \nabla^2 \mathbf{E}_L - \frac{\delta n_s}{2n_0} \mathbf{E}_L &= \frac{\delta n_{s, new}}{2n_0} \mathbf{E}_L \\ &= -\frac{\omega_{pe}}{12} \sum_k \frac{|\delta n_s^k|^2}{n_0^2 k^2 \lambda_{De}^2} \left(1 + i \frac{2}{3} \frac{\gamma_k}{\omega_{pe} k^2 \lambda_{De}^2} \right) \mathbf{E}_L, \quad [12] \end{aligned}$$

where γ_k is the damping rate of short-wavelength Langmuir wave with wavenumber k . The first term on the right-hand side of Eq. 12 is the frequency shift of a plain Langmuir wave by the scattering of the ion density fluctuations driven by short-wavelength IAWs. The second term corresponds to the damping of long-wavelength Langmuir waves due to their conversion to short-wavelength IAWs. The frequency shift is

$$\delta\omega = -\frac{\omega_{pe}}{12} \sum_k \frac{|\delta n_s^k|^2}{n_0^2 k^2 \lambda_{De}^2}. \quad [13]$$

This shift is the same for the entire Langmuir wavepacket spectrum and has no influence on the modulational instability.

After each LC, the frequency of the new Langmuir wave will decrease by a shift $\approx \omega_{pe} n_s^2 / n_0^2 / 12 \approx 0.01 \omega_{pe}$ assuming $k\lambda_{De} \approx 1$. We assume that the interval for LC is comparable to the time scale of modulational instability $100\omega_{pe}^{-1}$; the whole simulation is about $10,000 \omega_{pe}^{-1}$. Thus, the total frequency shift is about ω_{pe} . This agrees with what is shown in Fig. 2 in which Langmuir wave finally shifts to $k\lambda_{De} \ll 1$.

Concluding Remarks

PIC simulations were conducted to explore how the evolution of the strong ETSI produces Langmuir waves and plasma

coherent emission. We found that LC plays a critical role in the process, which enables regeneration of Langmuir waves and maintains a feedback loop for emission beyond the linear ETSI saturation (Fig. 1). The onset of LC is introduced by the $L-L$ wave coupling at the ETSI linear saturation stage and maintained by $L-W_s$ coupling from the nonlinear decay stage to the nonlinear saturation. The low-frequency KAWs and whistler waves generated near the ETSI peak finally reach equilibrium with the non-Maxwellian electron velocity distribution function (e.g., core-halo structure), as found in previous studies (19, 21).

In our simulations, the ETSI nonlinear saturation time is $\sim 1.5 \times 10^4 \omega_{pe}^{-1}$. Because the modulational instability nearly dominates the entire process, the nonlinear saturation time is approximately proportional to $(m_i/m_e)^{1/2}$, and, for the physical mass ratio, the ETSI nonlinear saturation time should be $\sim 10^5 \omega_{pe}^{-1}$, which is significantly longer than the ETSI linear saturation time $(n_0/n_b)^{1/3} \omega_{pe}^{-1} \approx 2\omega_{pe}^{-1}$. Note that our simulation assumes instantaneous injection of the electron beam, whereas, in the corona, the electron acceleration time is finite and the beam will propagate out of the region of initial generation. The acceleration time also affects the actual duration of the bursts (28, 29). The overall scenario is that coronal bursts produce nonthermal electrons that escape into space and produce interplanetary bursts (3) with accompanying waves. Our simulation assumes the beam energy is about 100 times that of the coronal thermal energy. For nanoflares, the beam energy is about a few kiloelectron volts if the corona temperature is ~ 10 eV. For flares, the electron beam energy can reach about a few megaelectron volts. The larger beam energy will change the results slightly because the ETSI growth rate does not rely on the velocity once the threshold is reached, but the turbulence becomes stronger and the decay lasts longer. On the other hand, we can estimate the emission power from Fig. 3B–D, in which the intensity ratio of the E_y of the radiation and the Langmuir wave is about 0.01 to 0.001, and thus the emission power is about a factor of 10^{-4} to 10^{-6} of the Langmuir wave power. Such energy loss is negligible dynamically. Therefore, the mechanism we have explored can provide a complete and self-consistent solution to the long-standing puzzle of why the duration of solar radio bursts is much longer than the linear saturation time of the ETSI [“Sturrock’s dilemma”(30)].

The short-wavelength IAWs and ion cavitons are two characteristics of LC, and can be detected by in situ solar wind observations. In particular, the forthcoming Solar Probe Plus mission will be capable of in situ detection of such radiation at $10 R_{\odot}$ from the Sun. The newly launched Magnetospheric Multiscale Mission is capable of in situ detections of Langmuir waves and cavitons in magnetosphere and solar wind at 1 AU.

We summarize some basic observations, which are consistent with our model predictions, in Table 1.

ACKNOWLEDGMENTS. H.C. and P.H.D. thank participants for discussions in the “8th Festival de Théorie,” Aix-en-Provence, France, 2015. P.H.D. thanks M. Malkov for discussions. This work was supported by the NASA Magnetospheric Multiscale Mission in association with NASA Contract NNG04EB99C (to H.C.) and Department of Energy Grant DE-FG02-04ER54738 (to P.H.D.). The simulations and analysis were carried out at the NASA Advanced Supercomputing facility at Ames Research Center under NASA High-End Computing Program Awards SMD-14-4848 and SMD-15-5715.

1. Wild JP, Smerd SF, Weiss AA (1963) Solar bursts. *Annu Rev Astron Astrophys* 1:291–366.
2. Saint-Hilaire P, Benz AO (2002) Energy budget and imaging spectroscopy of a compact flare. *Sol Phy* 210:287–306.
3. Aschwanden MJ (2002) Particle acceleration and kinematics in solar flares - A synthesis of recent observations and theoretical concepts (Invited Review). *Space Sci Rev* 101:1–227.
4. Saint-Hilaire P, Vilmer N, Kerdran A (2012) A decade of solar Type III radio bursts observed by the Nançay Radioheliograph 1998–2008. *Astrophys J* 762:60.
5. Ginzburg VL, Zhelezniakov VV (1959) On the mechanisms of sporadic solar radio emission. *IAU Symposium*, ed Bracewell RN (Int Astron Union, Paris), Vol 9, p 574.
6. Robinson PA (1997) Nonlinear wave collapse and strong turbulence. *Rev Mod Phys* 69:507–573.
7. Papadopoulos K, Goldstein ML, Smith RA (1974) Stabilization of electron streams in type III solar radio bursts. *Astrophys J* 190:175–186.
8. Smith RA, Goldstein ML, Papadopoulos K (1979) Nonlinear stability of solar type III radio bursts. I. Theory. *Astrophys J* 234:348–362.
9. Goldman MV, Reiter GF, Nicholson DR (1980) Radiation from a strongly turbulent plasma: Application to electron beam-excited solar emissions. *Phys Fluid* 23:388–401.
10. Sagdeev RZ, Galeev AA (1969) *Nonlinear Plasma Theory* (Benjamin, New York).
11. Rudakov LI, Tsytovich VN (1978) Strong Langmuir turbulence. *Phys Rep* 40:1–73.
12. Zakharov VE (1972) Collapse of Langmuir waves. *Sov J Exp Theor Phys* 35:908–914.
13. Papadopoulos K, Freund HP (1978) Solitons and second harmonic radiation in type III bursts. *Geophys Res Lett* 5:881–884.
14. Wong AY, Cheung PY (1984) Three-dimensional self-collapse of Langmuir waves. *Phys Rev Lett* 52:1222–1225.
15. Kellogg PJ, Goetz K, Howard RL, Monson SJ (1992) Evidence for Langmuir wave collapse in the interplanetary plasma. *Geophys Res Lett* 19:1303–1306.
16. Ergun RE, et al. (2008) Eigenmode structure in solar-wind Langmuir waves. *Phys Rev Lett* 101:051101.
17. Thejappa G, MacDowall RJ, Bergamo M (2013) Observational evidence for the collapsing Langmuir wave packet in a solar type III radio burst. *J Geophys Res* 118:4039–4052.
18. Dennis BR, Emslie AG, Hudson HS (2011) Overview of the volume. *Space Sci Rev* 159:3–17.
19. Che H, Goldstein ML, Viñas AF (2014) Bidirectional energy cascades and the origin of kinetic Alfvénic and whistler turbulence in the solar wind. *Phys Rev Lett* 112:061101.
20. Che H (2016) Electron two-stream instability and its application in solar and heliophysics. *Mod Phys Lett A* 31:1630018.
21. Che H, Goldstein ML (2014) The origin of non-Maxwellian solar wind electron velocity distribution function: Connection to nanoflares in the solar corona. *Astrophys J* 795:L38.
22. Stix TH (1992) *Waves in Plasmas* (Springer, New York).
23. Che H, Drake JF, Swisdak M, Goldstein ML (2013) The adiabatic phase mixing and heating of electrons in Buneman turbulence. *Phys Plasmas* 20:061205.
24. Gary SP (1993) *Theory of Space Plasma Microinstabilities* (Cambridge Univ Press, Cambridge, UK).
25. Melrose DB (1980) The emission mechanisms for solar radio bursts. *Space Sci Rev* 26:3–38.
26. Diamond PH, Itoh S-I, Itoh K (2014) *Modern Plasma Physics* (Cambridge Univ Press, Cambridge, UK).
27. Galeev AA, Sagdeev RZ, Shapiro VD, Shevchenko VI (1976) Effect of acoustic turbulence on the collapse of Langmuir waves. *Sov J Exp Theor Phys Lett* 24:21–24.
28. Goldstein ML, Smith RA, Papadopoulos K (1979) Nonlinear stability of solar type III radio bursts. II - Application to observations near 1 AU. *Astrophys J* 234, 683–695.
29. Ratcliffe H, Kontar EP, Reid HAS (2014) Large-scale simulations of solar type III radio bursts: Flux density, drift rate, duration, and bandwidth. *Astron Astrophys* 572:A111.
30. Sturrock PA (1964) Type III solar radio bursts. *NASA Spec Publ* 50:357–361.
31. Aschwanden MJ, Benz AO, Dennis BR, Schwartz RA (1995) Solar electron beams detected in hard X-rays and radio waves. *Astrophys J* 455:347–365.
32. Kellogg PJ, et al. (1992) Low frequency magnetic signals associated with Langmuir waves. *Geophys Res Lett* 19:1299–1302.
33. MacDowall RJ, et al. (1996) ULYSSES spacecraft observations of radio and plasma waves: 1991–1995. *Astron Astrophys* 316:396–405.
34. Lin RP, Potter DW, Gurnett DA, Scarf FL (1981) Energetic electrons and plasma waves associated with a solar type III radio burst. *Astrophys J* 251:364–373.
35. Thejappa G, MacDowall RJ (2004) High frequency ion sound waves associated with Langmuir waves in type III radio burst source regions. *Nonlinear Process Geophys* 11:411–420.